Light | Advanced Manufacturing
Sister Journal of Light | Science & Applications

Supplementary Materials for

- **Full title: Precise motion tracking and velocimetry using chirped power oscillation wave**

Wei Du, Yujia Li, Hao Wu, Lei Chen, Lei Gao, Dongmei Huang, Leilei Shi, Wei Gao, Lei Wei, Baicheng Yao, Tao Zhu

* liyujia@cqu.edu.cn; yaobaicheng@uestc.edu.cn; zhutao@cqu.edu.cn

This PDF file includes:

Supplementary Text

Figs. S1 to S6

Supplementary Text

S1. The specific process of dispersion control

We conducted a simulation of the proposed distance measurement method using nonlinear Schrödinger equation (NLSE):

$$\frac{\partial A}{\partial z} = -\frac{\alpha}{2}A - i\frac{\beta_2}{2}\frac{\partial^2 A}{\partial T^2} + \frac{\beta_3}{6}\frac{\partial^3 A}{\partial T^3} + i\gamma\left|A\right|^2 A, \qquad (S.1)$$

where the value of α is set to 0. Based on dispersion control, the relevant parameters were set as follows. The pulse width of the ultrafast laser was 5 ps, the length of the dispersion-compensating fiber in the first segment for pulse stretching was 7400 m. For DCF1, its second-order and third-order dispersion coefficients (β_2, β_3) were 0.2546×10^{-24} s^2 m^{-1} and -0.1425×10^{-39} s^3 m^{-1}, respectively. The temporal evolution of the measurement arm's signal optical pulse as it propagates through the 7400 m-long DCF1 is shown in Fig. S1(a). The length of the dispersion-compensating fiber introduced in the reference arm was 105 m. For DCF2, its second-order and third-order dispersion coefficients (β_2, β_3) were 0.3346×10^{-24} s^2 m^{-1} and -0.1456×10^{-39} s^3 m^{-1}, respectively. The temporal evolution of the reference arm's signal optical pulse as it propagates through the 7400 m-long DCF1 and the 105 m-long DCF2 is shown in Fig. S1(b). The pulse shape of the two interferometric arm's optical signals after dispersion control are shown in Fig. S1(c), the two pulses exhibit a slight difference in pulse widths. Additionally, to simulate realistic experimental conditions, we incorporated noise arising from the fiber and the detector into the simulation. The interferometric signals and the sweep frequency curves of the two interferometric arm's optical signals when the measured distance is 0, which are shown in Fig. S1(d). It is clearly evident that the intersection point of the two frequency-swept curves coincides with the ZFP.

S2. The theoretical speed limit

According to our manuscript, the phase in the interference signal, which is induced by the rapid motion of the target, can be extracted through the power oscillation wave. This phase can be expressed as

$$\varphi = \omega_0 \tau \tag{S.2}$$

where ω_0 denotes the central angular frequency of the light source, and τ represents the corresponding time delay. The phase at the N instant is given by

$$\varphi(N) = \frac{2\omega_0 L_N}{c} \tag{S.3}$$

Here, L_N represents the distance corresponding to the target at the N instant, and c denotes the speed of light. The phase at the N+1 instant is given by

$$\varphi(N+1) = \frac{2\omega_0 L_{N+1}}{c} \tag{S.4}$$

where L_{N+1} denotes the distance corresponding to the N+1 instant. Based on the periodicity of the triangular wave and the Nyquist sampling theorem, the phase difference between two adjacent instants should be less than π,

$$\varphi(N+1) - \varphi(N) = \frac{2\omega_0 (L_{N+1} - L_N)}{c} < \pi \tag{S.5}$$

At this point, the velocity of the target can be expressed as

$$v = \frac{(L_{N+1} - L_N)}{\Delta t} = (L_{N+1} - L_N) f_{rep} < \frac{\pi c f_{rep}}{2\omega_0} = \frac{c f_{rep}}{4 f_0} \tag{S.6}$$

Here, Δt represents the time interval between light pulses, f_{rep} denotes the repetition rates of the ultrafast pulsed laser used, and f_0 is its central frequency. Therefore, the measurable theoretical speed limit of the proposed method can be expressed as

$$v_{\max} = \frac{c f_{rep}}{4 f_0} \tag{S.7}$$

We have verified the effectiveness and accuracy of the proposed speed measurement method through numerical simulations. Additionally, we simulated the corresponding speed limits under different repetition frequencies of ultrafast pulsed lasers and compared the results with theoretical values, as shown in Figs. S3 and S4. Figures S2(a) and S2(b) present the speed

measurement results when the phase difference between two adjacent instants is less than π with light source repetition rates of 7.7 MHz. Figure S2(c) illustrates the phase jump phenomenon in the interference signal when the phase difference exceeds π, which leads to jumps in the simulation results, as shown in Fig. S2(d). This further confirms the theoretical speed limit of the proposed method. Figure S3 displays the interference signal color maps and speed measurement results under different repetition rates of the light source (7.7 MHz, 77 MHz, 200 MHz, 300 MHz, 500 MHz). From Figs. S4(a) and S4(b), we observe that the results obtained from numerical simulations are almost consistent with the theoretical speed limit, approximately 95% of the theoretical limit. Figure S4(c) shows the relative error values of the simulated measurements at different set speeds, including the average relative error and maximum relative error. The average relative error at each speed is less than 0.01%, and the maximum relative error is around 0.035%, which thoroughly validates the superior speed measurement accuracy of the proposed method. Figure S4(d) presents the standard deviation of the absolute error of the simulation results at five different speeds compared to the set speeds, further demonstrating the stability of the method for speed measurement.

Indeed, increasing the repetition rate toward the 200 MHz level would impose more stringent requirements on both the photodetector and the data acquisition electronics. Specifically, the photodetector would need to maintain sufficient bandwidth and linearity to accurately capture the higher-frequency components of the interference signal, while the oscilloscope or digitizer would require a correspondingly higher sampling rate and memory bandwidth to faithfully record the temporal dynamics without aliasing or signal distortion. In addition, electronic noise, jitter, and thermal effects could become more pronounced at elevated repetition rates, potentially limiting the achievable signal-to-noise ratio (SNR) and overall measurement fidelity. These considerations represent the primary hardware bottlenecks in scaling the system. In fact, as mentioned above, the proposed method only requires detecting the portion of the signal near the ZFP in the interference signal, which imposes lower bandwidth requirements compared to the fast Fourier transform (FFT)-based methods.

S3. The impact of noise

To investigate the impact of source noise, photodetector noise, and environmental noise on the maximum measurable speed, we performed simulations of the maximum measurable speed under different SNRs (20 dB, 40 dB, 60 dB, 80 dB) when the light source repetition rates is 7.7 MHz. In a real experimental environment, low-frequency noise generated by factors such as temperature and humidity, as well as high-frequency noise from the light source and photodetector, ultimately affect the experimental results. Therefore, in the simulation, white noise is introduced, which encompasses both low-frequency and high-frequency noise, and the results are shown in Fig. S5. It is clearly observed that as the SNR increases, the phase noise in the interference signal decreases, leading to an increase in the final maximum measurable speed. When the SNR is 80 dB, the maximum measurable speed reaches 99.7% of the theoretical speed limit.

S4. The velocity measurement impact of the Doppler frequency shifts effect

Most existing speed measurement methods are based on the Doppler shifts phenomenon. Therefore, it is essential to investigate the impact of Doppler shifts on the proposed method while using it for speed measurement. We further incorporated the Doppler shifts induced by the high-speed motion of the target into our simulation experiments,

$$\omega = \omega_0 \left[\left(c - v \right) \ / \ \left(c + v \right) \right]^{1/2} \tag{S.8}$$

where ω_0 is the frequency of emitted light, ω is the frequency of reflected light, and v is the velocity of moving target. The signals of both arms at this moment can be represented as follows.

$$\begin{aligned} E_1(t) &= A_1(t) e^{-i(\omega t + \pi k_1 t^2)}, \\ E_2(t) &= A_2(t) e^{-i(\omega t + \pi k_2 t^2)} \end{aligned} \tag{S.9}$$

The simulation results are shown in Fig. S6. We assess the impact of Doppler shifts on the speed measurement performance of the proposed method by examining the maximum measurable speed, standard deviation, average relative error, and maximum relative error. The simulation results indicate that the Doppler shifts have minimal effect on the measurement accuracy and stability of the proposed method, with only a slight impact on the maximum measurable speed, which does not exceed 0.4%.

S5. The target objects and application scenarios corresponding to typical speeds

In the field of high-precision machining and advanced precision equipment, different motion speed regimes correspond to distinct application scenarios and target objects, reflecting the trade-off between positioning accuracy, dynamic response, and system stability, as shown in Table 1. At low speeds around 20 mm s^{-1}, the focus is typically on ultraprecision positioning and nano-scale machining, such as in semiconductor lithography stages, atomic force microscope (AFM) nanopositioners, and ultraprecision diamond turning systems, where nanometer-level accuracy and sub-nanometer vibration control are critical. Medium-speed operation around 3 m s^{-1} is characteristic of high-precision servo motion and contour machining, including high-speed micro-milling, laser microfabrication, and precision robotic assembly, where maintaining sub-micron trajectory accuracy under dynamic conditions is essential. In contrast, high-speed motion near 30 m s^{-1} is associated with ultrafast scanning and high-dynamic-response systems, such as galvanometric scanners, high-speed spindles, and laser beam steering devices, which demand excellent dynamic stiffness, thermal stability, and vibration suppression at extreme accelerations.

Table 1 The target objects and application scenarios corresponding to typical speeds.

Typical speeds	Application scenarios	Target objects
Low speeds (~20 mm s^{-1})	Ultraprecision positioning and nano-scale machining	Semiconductor lithography stages, atomic force microscope (AFM) nanopositioners, and ultraprecision diamond turning systems
Medium speeds (~3 m s^{-1})	High-precision servo motion and contour machining	High-speed micro-milling, laser microfabrication, and precision robotic assembly
High speeds (~30 m s^{-1})	Ultrafast scanning and high-dynamic-response systems	Galvanometric scanners, high-speed spindles, and laser beam steering devices

Figures

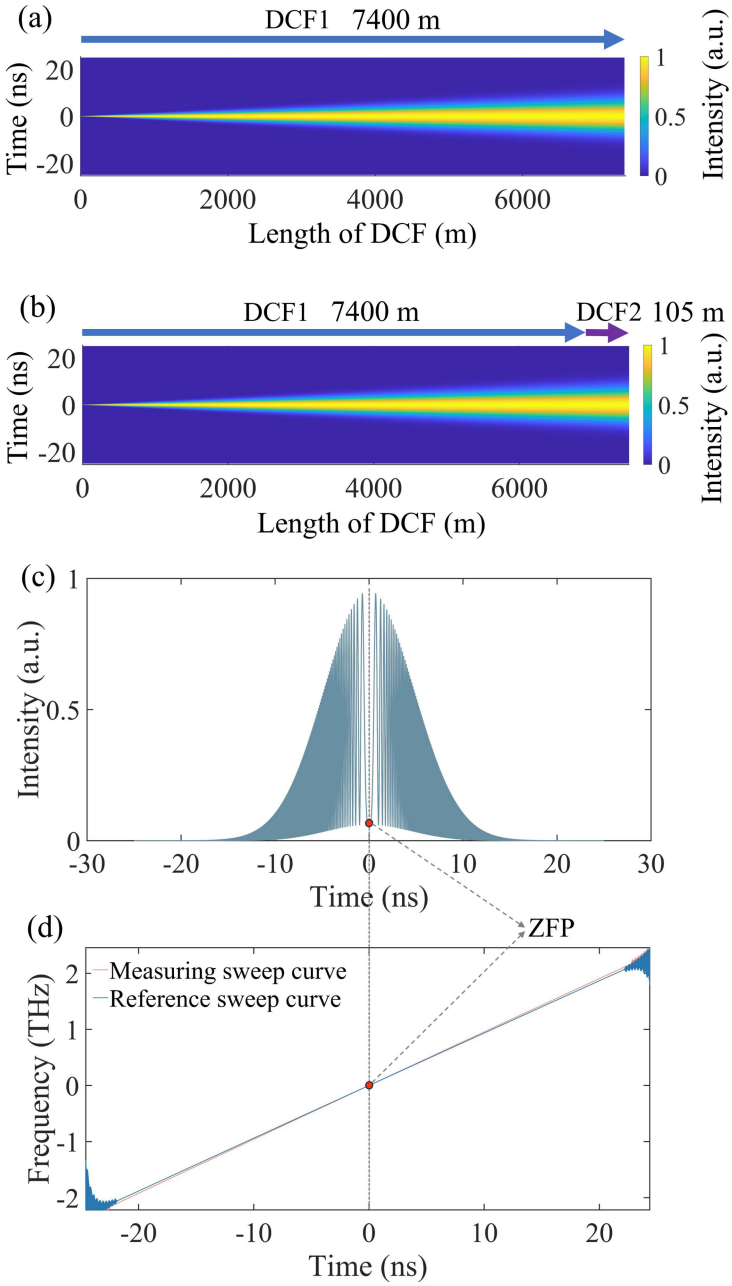

Fig. S1. Dispersion controlling process of the dual-sweep frequency laser. (a) The temporal evolution of the measurement arm's signal optical pulse as it propagates through the 7400 m-long DCF1. (b) The temporal evolution of the reference arm's signal optical pulse as it propagates through the 7400 m-long DCF1 and the 105 m-long DCF2. (c) The interferometric signal. (d) The sweep frequency curves of the two interferometric arm's optical signals when the measured distance is 0.

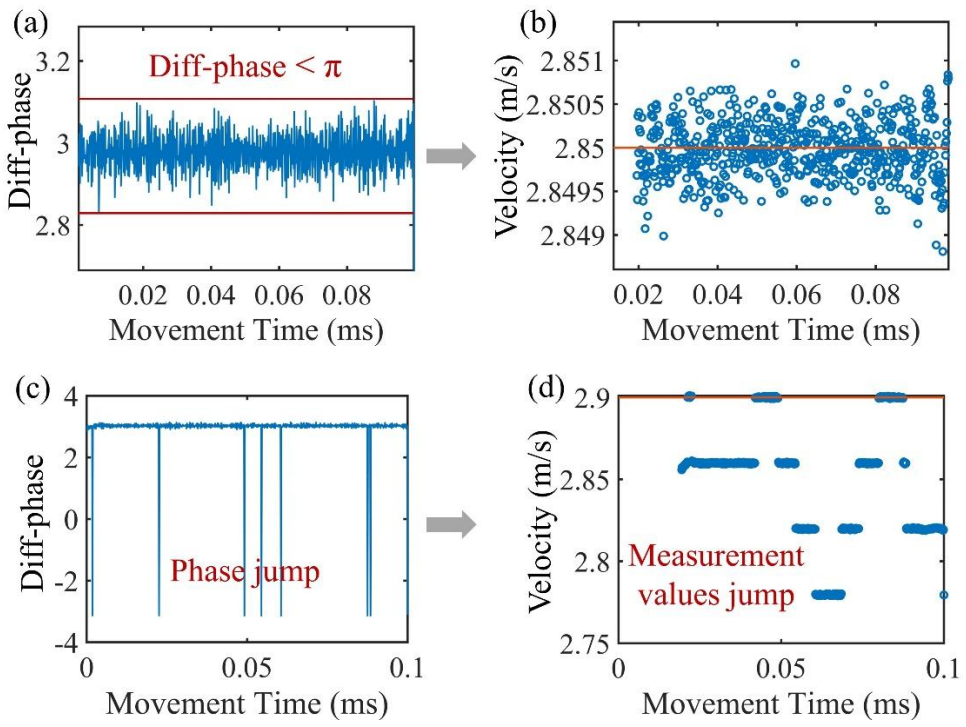

Fig. S2. The source of the velocimetry theoretical limitation. (a) The phase change of the interference signal detected by a target with a tracking speed of 2.85 m s^{-1} when the repetition rate of the light source is 7.7 MHz. (b) When the repetition rate of the light source is 7.7 MHz, the detected velocity of the target moving at a speed of 2.85 m s^{-1}. (c) The phase change of the interference signal detected by a target with a tracking speed of 2.9 m s^{-1} when the repetition rate of the light source is 7.7 MHz. (d) When the repetition rate of the light source is 7.7 MHz, the detected velocity of the target moving at a speed of 2.9 m s^{-1}.

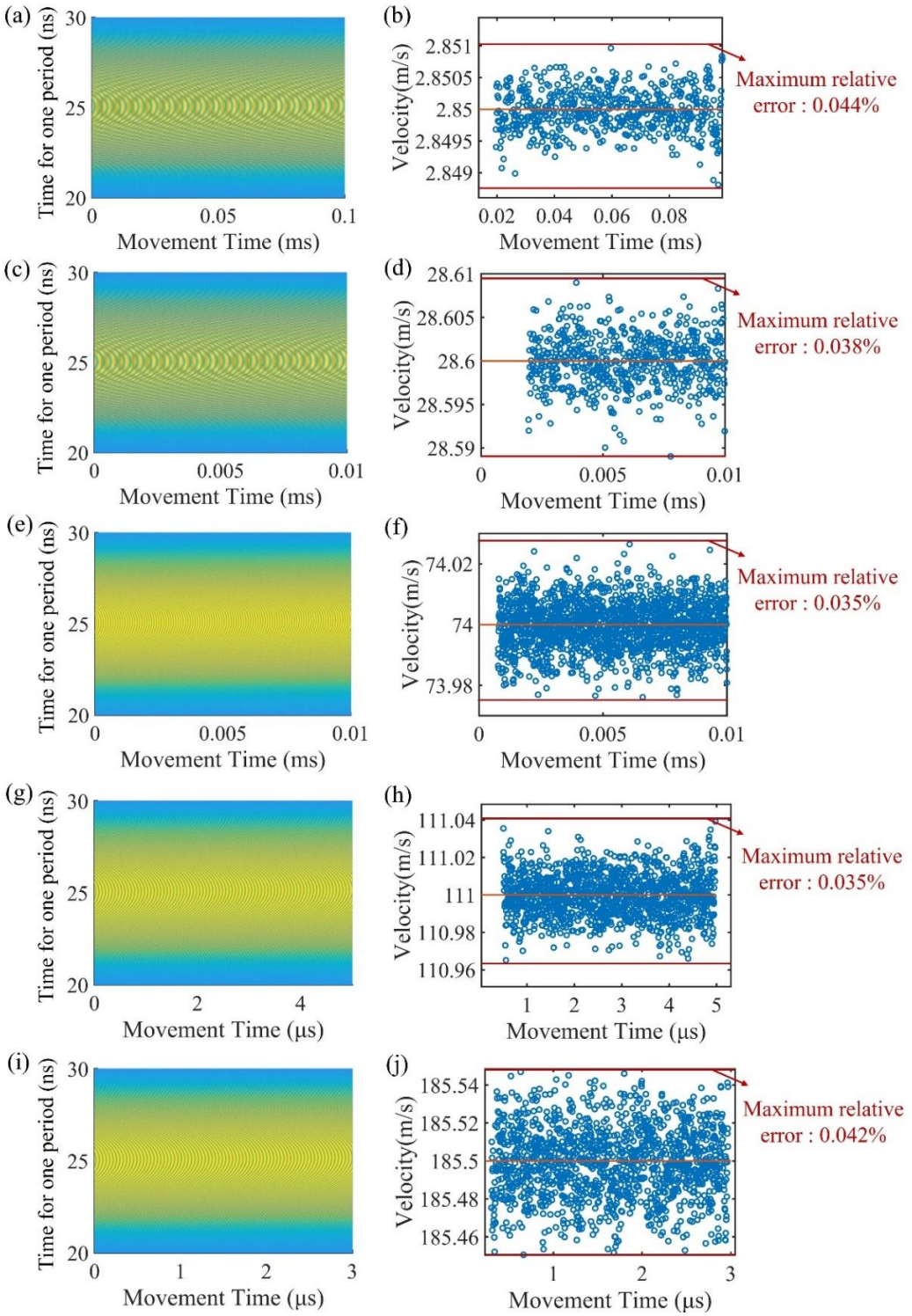

Fig. S3. The maximum simulated velocity measurements at five different light source repetition rates (7.7 MHz, 77 MHz, 200 MHz, 300 MHz and 500 MHz) and the corresponding color maps.

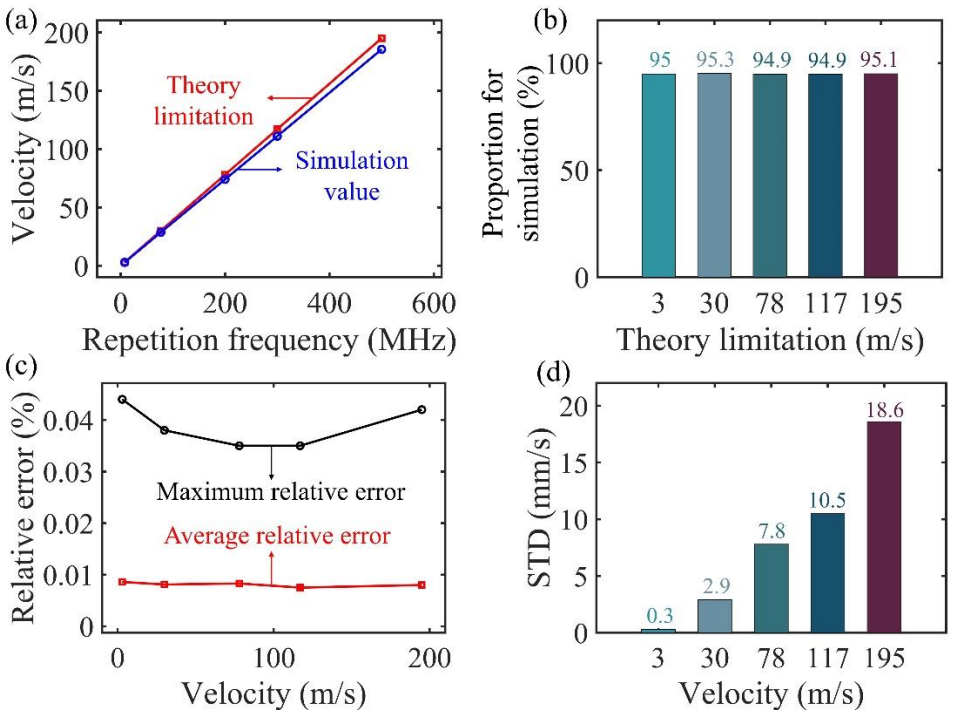

Fig. S4. The simulated velocity measurement results at five different light source repetition rates. (a) Comparison between the simulated values and the theoretical limitations. (b) The percentage of simulated values relative to the theoretical limitations. (c) The maximum relative error and the average relative error of the simulated velocity measurements. (d) The standard deviation of the simulated velocity measurements.

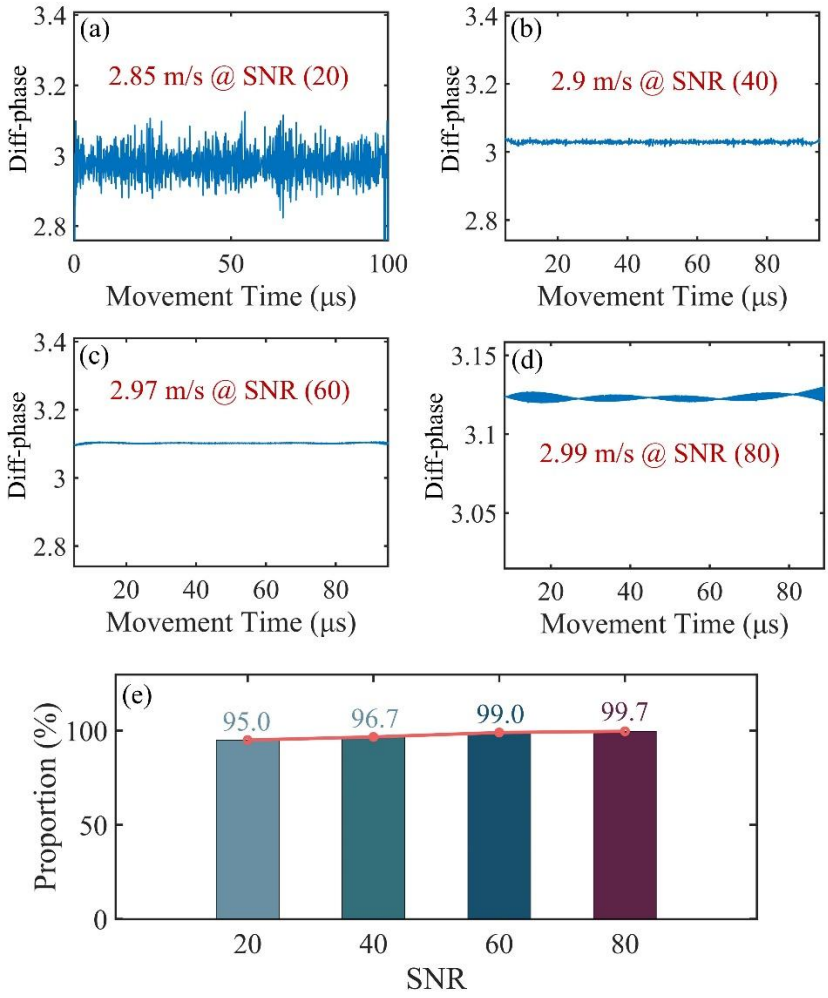

Fig. S5. Phase fluctuation under different SNRs and the simulated maximum velocity measurement.

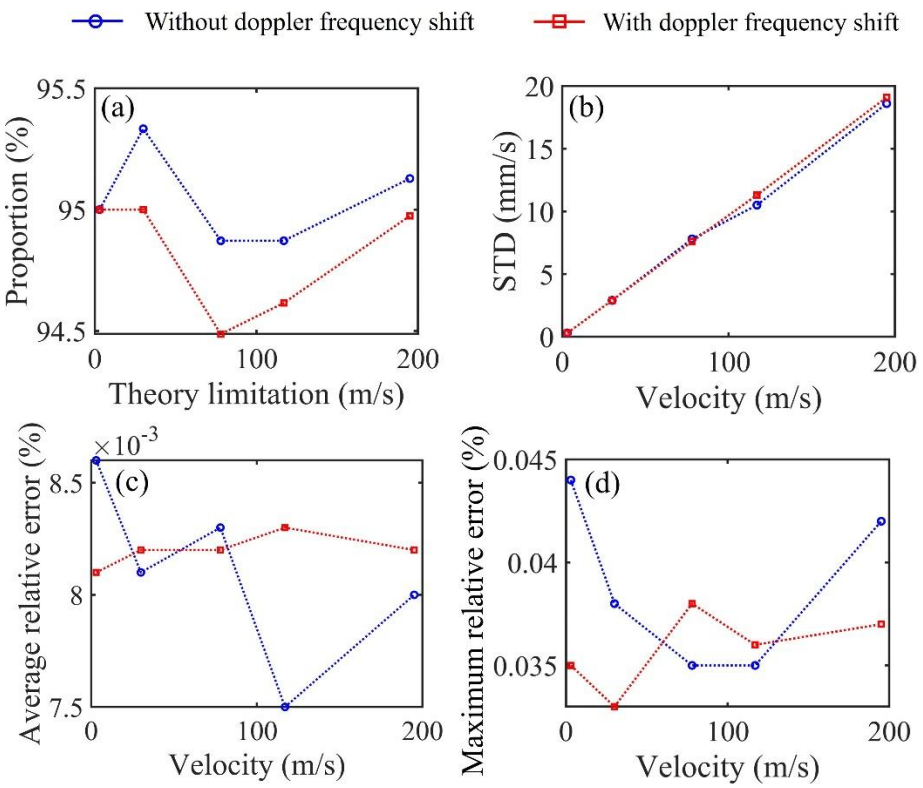

Fig. S6. Consideration of the simulated velocity measurement results under the Doppler frequency shifts effect, including the maximum measurable value, standard deviation, average relative error, and maximum relative error.